Title
The Role of Alkalis in Orchestrating Uranyl-Peroxide Reactivity Leading to Direct Air Capture of Carbon Dioxide

Journal
Chemistry - A European Journal, 30(27)

ISSN
0947-6539

Authors
Arteaga, Ana
Arino, Trevor
Moore, Guy C
et al.

Publication Date
2024-05-14

DOI
10.1002/chem.202301687

Peer reviewed

Chemistry–A European Journal
Research Article
doi.org/10.1002/chem.202301687
Chemistry Europe
European Chemical Societies Publishing
www.chemeurj.org

The Role of Alkalis in Orchestrating Uranyl-Peroxide Reactivity Leading to Direct Air Capture of Carbon Dioxide

Ana Arteaga,[a, b] Trevor Arino,[a, c] Guy C. Moore,[d, e] Jenna L. Bustos,[a] Matthew K. Horton,[d, e] Kristin A. Persson,[d, f] Jun Li,[a] William F. Stickle,[g] Tsuyoshi A. Kohlgruber,[b] Robert G. Surbella, III,[b] and May Nyman*[a]

Spectator ions have known and emerging roles in aqueous metal-cation chemistry, respectively directing solubility, speciation, and reactivity. Here, we isolate and structurally characterize the last two metastable members of the alkali uranyl triperoxide series, the Rb^+ and Cs^+ salts (Cs-$\mathbf{U_1}$ and Rb-$\mathbf{U_1}$). We document their rapid solution polymerization via small-angle X-ray scattering, which is compared to the more stable Li^+, Na^+ and K^+ analogues. To understand the role of the alkalis, we also quantify alkali-hydroxide promoted peroxide deprotonation and decomposition, which generally exhibits increasing reactivity with increasing alkali size. Cs-$\mathbf{U_1}$, the most unstable of the uranyl triperoxide monomers, undergoes ambient direct air capture of CO_2 in the solid-state, converting to $Cs_4[U^{VI}O_2(CO_3)_3]$, evidenced by single-crystal X-ray diffraction, transmission electron microscopy, and Raman spectroscopy. We have attempted to benchmark the evolution of Cs-$\mathbf{U_1}$ to uranyl tricarbonate, which involves a transient, unstable hygroscopic solid that contains predominantly pentavalent uranium, quantified by X-ray photoelectron spectroscopy. Powder X-ray diffraction suggests this intermediate state contains a hydrous derivative of CsU^VO_3, where the parent phase has been computationally predicted, but not yet synthesized.

Introduction

Peroxide is a unique ligand that enables solubilization of high-valent metal cations in base, including the early d^0 transition metals and f^0 actinides, and can also serve as either a reducing or oxidizing agent. Peroxide has a unique affinity for binding the uranyl cation, UO_2^{2+}, and this is exploited in uranium mining to form studtite (simultaneous solubilization and oxidation of U^{IV} to UO_2^{2+}).[1] Studite is also found in weathered uranium deposits, where the peroxide is generated by α-radiolysis of water.[2] Uranyl dissolved in organic solutions without peroxide photochemically yields uranyl peroxide complexes, evidenced by crystallization.[3] These cases of in situ generated peroxides to form uranyl peroxide phases, by either radiolysis or some other means, highlights the unique affinity of peroxide for the uranyl cation, and also uranium's photochemical and redox behavior.

Exploiting the stability and solubility of uranyl peroxide species, uranyl polyoxometalate capsules were first synthesized in 2005.[4] This newest polyoxometalate family has grown to include many unique cluster topologies with hydroxyl, peroxide, oxalate, and pyrophosphate ligands.[5] Important members of the family include $\mathbf{U_{60}}$ akin to $\mathbf{C_{60}}$; $\mathbf{U_{20}}$, one of the five platonic solids with its 12 pentagonal faces;[6] and $\mathbf{U_{24}}$ with the sodalite-like topology that is also featured in imidazolate metal-organic frameworks.[4,7] Computational and experimental studies evidence their universally recognized symmetries are influenced by alkali-countercations present during self-assembly, wherein topological faces are commensurate with alkali size.[8] These topological faces include squares ($\mathbf{U_4}$ templated by Li^+),[9] pentagons ($\mathbf{U_5}$ templated by Na^+ and K^+),[6a,8c] and hexagons ($\mathbf{U_6}$ templated by K^+, Rb^+, and Cs^+).[8c,10]

Prior, we observed the self-assembly of uranyl peroxide clusters in solution from $\mathbf{U_1}$ to $\mathbf{U_5}$ and $\mathbf{U_6}$ faces via small-angle X-ray scattering (SAXS), and isolated them by crystallization.[11] This could not be achieved in a controlled manner without first stabilizing the very reactive K^+ salt of the uranyl triperoxide monomer ($K_4[UO_2(O_2)_3]$, K-$\mathbf{U_1}$, Figure 1c). This was accomplished by isolating K-$\mathbf{U_1}$ as a crude solid, followed by solid-to-solid crystallization in vacuo.[11a,12] In contrast, the Li-$\mathbf{U_1}$ and Na-$\mathbf{U_1}$ (Figure 1a, 1 b) salts are readily synthesized and stable.[13] In fact, Li-$\mathbf{U_1}$ is stable in solution for weeks, without the presence of a redox-active metal to catalyze the peroxide decomposition.[9a] In sum, prior observations showed reactivity of $\mathbf{U_1}$ in solution and

[a] Dr. A. Arteaga, T. Arino, J. L. Bustos, Dr. J. Li, Prof. Dr. M. Nyman
Department of Chemistry, Oregon State University, Corvallis, OR, 97331 USA
E-mail: may.nyman@oregonstate.edu
[b] Dr. A. Arteaga, Dr. T. A. Kohlgruber, Dr. R. G. Surbella, III
Pacific Northwest National Laboratory, 902 Battelle Blvd, Richland, WA 99354 USA
[c] T. Arino
current address: Department of Nuclear Chemistry U.C. Berkeley, Berkeley, California 94720 USA
[d] G. C. Moore, Dr. M. K. Horton, Prof. Dr. K. A. Persson
Department of Materials Science and Engineering, U. C. Berkeley, California, 94720, USA
[e] G. C. Moore, Dr. M. K. Horton
Materials Science Division, Lawrence Berkeley National Laboratory, Berkeley, CA 94720, USA
[f] Prof. Dr. K. A. Persson
Molecular Foundry, Lawrence Berkeley National Laboratory, Berkeley, CA 94720, USA
[g] Dr. W. F. Stickle
Hewlett-Packard, Inc, 1040 NE Circle Blvd, Corvallis, OR 97330 USA
Supporting information for this article is available on the WWW under https://doi.org/10.1002/chem.202301687

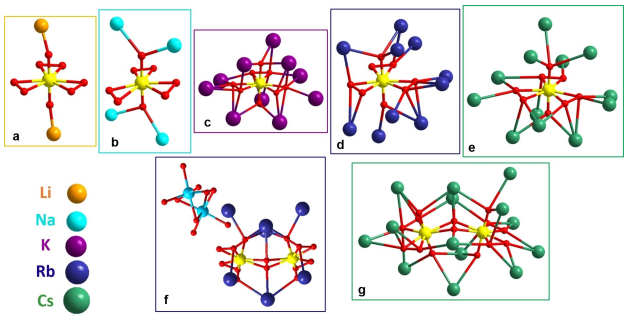

Figure 1. Summary of $\mathbf{U}_1$ and $\mathbf{U}_2$ structures emphasizing the trend of increasing direct bonding of alkalis to the uranyl peroxide anionic unit with increasing alkali size. a) Li-$\mathbf{U}_1$,[18] b) Na-$\mathbf{U}_1$,[13a] c) K-$\mathbf{U}_1$,[12] d) Rb-$\mathbf{U}_1$, e) Cs-$\mathbf{U}_1$, f) NaRb-$\mathbf{U}_2$, g) Cs-$\mathbf{U}_2$.

the solid-state increases with alkali cation size from Li^+ to K^+.[9a,11a]

The alkali-dependent reactivity is poorly understood because alkali cations have no well-established role in aqueous chemistry, aside from structural templating and orchestrating solubility. Moreover, computational studies do not necessarily provide insight, since their speciation does not change from reactant to product. The conversion of $\mathbf{U}_1$ to capsules requires peroxide decomposition.[14] In alkaline conditions, peroxide decomposes via disproportionation; $O_2^{2-}{}_{(aq)} \rightarrow {}^1/_2O_{2(g)} + O^{2-}{}_{(aq)}$. Notably, if the peroxide acts as an oxidizing agent (most common in alkaline conditions), the O–O bond must break. On the other hand, peroxide can behave as a reducing agent without necessarily breaking the O–O bond; i.e. $O_2^{2-}{}_{(aq)} \rightarrow O_{2(g)} + 2e^-$.

Rb-$\mathbf{U}_1$ and Cs-$\mathbf{U}_1$ have not yet been reported, due to their exceedingly rapid decomposition upon attempting to isolate them as solids. Efforts to synthesize Rb-$\mathbf{U}_1$ or Cs-$\mathbf{U}_1$ by following the same synthetic procedures for stable Li-$\mathbf{U}_1$ or Na-$\mathbf{U}_1$ yields a bright yellow solid, which then rapidly degrades to a red, wet solid with observed bubble formation (peroxide decomposition) and polymerization (insolubility in water).

Here, we present a synthetic route and crystal structures of Rb-$\mathbf{U}_1$ and Cs-$\mathbf{U}_1$ (in addition to Rb-$\mathbf{U}_2$ and Cs-$\mathbf{U}_2$ dimers), completing the alkali-$\mathbf{U}_1$ series. X-ray scattering monitors the conversion of $\mathbf{U}_1$ to topological faces in water, defining a relationship between alkali size and reactivity, trending Cs-$\mathbf{U}_1$ > Rb-$\mathbf{U}_1$ > K-$\mathbf{U}_1$ > Na-$\mathbf{U}_1$ > Li-$\mathbf{U}_1$. By Raman spectroscopy, the AOH-driven (A = alkali) deprotonation and decomposition of peroxide identified the same general trend. Finally, the major solid-state decomposition product of unstable Cs-$\mathbf{U}_1$ was identified as cesium uranyl tricarbonate, $[Cs_4[UO_2(CO_3)_3]$ (Cs-$\mathbf{U}_{1c}$), (by single-crystal X-ray diffraction [SCXRD], Raman spectroscopy, and transmission electron microscopy [TEM]) via direct air capture (DAC) of CO_2. Attempts to track the reaction pathway and understand the role of the alkalis yielded three lines of evidence that a hydrous derivative the computationally predicted CsU^VO_3 compound[15] was among the hygroscopic, red material that forms from Cs-$\mathbf{U}_1$. This evidence includes 1) X-ray photoelectron spectroscopy (XPS) identifying pentavalent uranium, 2) an experimental diffraction pattern that is consistent with the computed CsU^VO_3 calculated diffractogram, and 3) Raman spectra consistent with U-O-U of a framework material. Based on this, we surmise that larger alkalis can accelerate peroxide decomposition; and in some instances, peroxide can act as a reducing agent. The intermediate state is short-lived and sometimes not observed.

Regardless, the end-product is crystalline $Cs_4[U^{VI}O_2(CO_3)_3]$, identified by diffraction and spectroscopic techniques. Recenty we also reported vanadium peroxide $V(O_2)_4^{3-}$ conversion to $VO(CO_3)(O_2)_2^{3-}$ via DAC, also with increasing reactivity with alkali counterion size: trending $K^+ < Rb^+ < Cs^+$.[16] Understanding these trends of peroxometalate DAC and the role of the alkalis adds to our knowledge of how to remove CO_2 from the atmosphere, arguably one of the most important reactions for a sustainable energy future.

Results and Discussion

Synthesis and Uranyl Peroxide Structures

Rb-$\mathbf{U}_1$ and Cs-$\mathbf{U}_1$ were synthesized by a method adapted from prior-reported K-$\mathbf{U}_1$,[12] and is summarized in the Supporting Information (SI). Briefly, in an ice bath, uranyl nitrate is precipitated as studtite by addition of peroxide. Upon addition of CsOH or RbOH, the solid redissolves and the solution rapidly goes from orange to yellow. Rapid addition of acetone once the yellow color is observed precipitates a yellow solid. This is then centrifuged, the liquid is decanted, and the solid is placed in a vacuum oven. The presumedly amorphous solid grows crystals over the course of several hours, which are of sufficient quality to analyze by SCXRD (Figure S1). The Raman spectra of the amorphous solids (Figure S2) indicate the presence of the uranyl triperoxide monomer. Rapid preciptation and low temperature throughout the synthesis is crucial to avoid polymerization of the uranyl peroxide monomers, which challenges crystallization of $\mathbf{U}_1$. Even with our extensive experience, this reaction has an ~30% success rate, evidencing instability of these compounds and their tendency to polymerize.

Rb-$\mathbf{U}_1$ ($Rb_4[UO_2(O_2)_3 \cdot 4H_2O$) crystallizes in the $P2_1/c$ space group (Tables S2–S4, Figure 1d). The $UO_2(O_2)_3^{4-}$ monomer exhibits the typical hexagonal bipyramidal geometry with U-O_{yl} bond distances of 1.849(6) Å and 1.841(6) Å. In the equatorial plane, the three peroxide (O_p) groups have U-O_p bond lengths between 2.296(6)–2.329(7) Å, and O_p-O_p bond lengths of 1.491(1)–1.536(1) Å. The four charge-balancing Rb^+-cations form multiple bonds with the $[UO_2(O_2)_3]^{4-}$ moiety, with bond lengths between 2.818(6)–3.559(7) Å. There are five Rb^+-O_{yl} bonds per anion and nine Rb^+-O_p bonds per anion. The experimental powder X-ray diffractogram of Rb-$\mathbf{U}_1$ is mostly consistent with the calculated pattern from the single-cystal experiment. However, the pattern shows signs of partial decomposition and/or dehydration, in addition to preferred orienation (Figure S3). This is typical of hydrous polyoxoanion salts.

Cs-$\mathbf{U_1}$ ($Cs_4[UO_2(O_2)_3]\cdot 12H_2O$,CsOH) crystallizes in the *P*-1 space group (Tables S2, S5, S6, Figure 1e). There are two unique $UO_2(O_2)_3^{4-}$ anions in the unit cell, with U-O_{yl} bond distances between 1.835(1)–1.858(2) Å. The U-O_p bond distances are between 2.280(2)–2.350(2) Å. Similar to Rb-$\mathbf{U_1}$, the Cs^+ cations are directly bonded to the $UO_2(O_2)_3^{4-}$ anion with bond lengths between 2.877(2)–3.784(2) Å, via five Cs^+-O_{yl} bonds for each crystallographically unique anion, and six and nine Cs^+-O_p bonds respectively for the two anions. Additionally, there are 12 lattice waters and one co-crystallized CsOH per formula unit. Notably, bulk characterization of Cs-$\mathbf{U_1}$ was not completed due to the reactivity of these crystals outside the mother liquor. The crystals degrade to form a hygroscopic red powder (Figure S1c).

NaRb-$\mathbf{U_2}$ ($Rb_4Na_2[(UO_2)_2(O_2)_5]\cdot 13H_2O$, $\mathbf{U_2}$ refers to a dimer) was obtained by dissolving Rb-$\mathbf{U_1}$ in water/peroxide and recrystallization (discussed later, see SI for details). NaRb-$\mathbf{U_2}$ crystallizes in the *Pbcm* space group (Tables S2, S7, S8, Figure 1f). The U-O_{yl} bond distance is 1.838(5) Å. The bridging U-O_p bond distances are 2.359(2) Å and 2.407(3) Å, and the terminal U-O_p bond distances are 2.270(5)–2.302(4) Å. The $[(UO_2)_2(O_2)_5]^{6-}$ dimer anion is charge-balanced with 4 Rb^+ and 2 Na^+ cations and there are 13 lattice waters per molecular unit. Like Rb-$\mathbf{U_1}$ and Cs-$\mathbf{U_1}$ there is extensive bonding between Rb^+ and the dimer anion (Figure 1f) with Rb-O_p and Rb-O_{yl} bonds with distances of 2.871(5)–3.509(6) Å. Inclusion of a common impurity such as Na^+ that inadvertently promotes crystallization is not unprecedented, and has been previously observed in the crystallization of the $[Nb_6O_{19}]^{8-}$ polyoxometalate from alkaline CsOH and RbOH solution.[17]

Cs-$\mathbf{U_2}$ ($Cs_6[(UO_2)_2(O_2)_5]\cdot 11H_2O$) was obtained in a similar manner as Cs-$\mathbf{U_1}$, but acetonitrile is used to precipitate the solid, instead of acetone (see SI for details). Cs-$\mathbf{U_2}$ crystallizes in the *P*-1 space group (Tables S2, S9, S10, Figure 1g). The dimeric unit is essentially identical to that of NaRb-$\mathbf{U_2}$. The U-O_{yl} distances are 1.824(2)–1.861(2) Å, bridging U-O_p bond distances are 2.360(1)–2.391(1) Å, and the terminal U-O_p bond distances are between 2.260(1)–2.326(1) Å. The $[(UO_2)_2(O_2)_5]^{6-}$ anion is charge-balanced with 6 Cs^+ cations and 12 lattice waters are located. Extensive bonding between Cs^+ and the dimeric anion is also observed in Cs-$\mathbf{U_2}$ with bond lengths of Cs-O_p and Cs-O_{yl} ranging from 2.935(21)–3.629(2) Å.

The bonding of peroxide and Rb^+ and Cs^+ in the $\mathbf{U_1}$ and $\mathbf{U_2}$ structures contrasts that of Li-$\mathbf{U_1}$[18] and Na-$\mathbf{U_1}$.[13] In Li-$\mathbf{U_1}$ and Na-$\mathbf{U_1}$, the alkalis bond only to the yl-oxos (Figure 1a–b). This perhaps gives some indication of the role of the alkalis in the starkly different solid-state reaction pathways and the reactivity of A-$\mathbf{U_1}$ in solution.

Solution Reactivity of A-$\mathbf{U_1}$

We have benchmarked the reactivity of the A-$\mathbf{U_1}$ monomer series in solution. SAXS and Raman spectroscopy were used to monitor the evolution of A-$\mathbf{U_1}$ to cluster intermediate faces, followed by the precipitation of capsules. Uranyl peroxide capsules are insoluble with heavier alkalis (Rb^+, Cs^+), like most polyoxometalates,[19] and therefore, we never observed capsules templated and charge-balanced by Rb^+ and Cs^+ in pure forms via SAXS. Nonetheless, they have been crystallized prior,[10] providing benchmarking characterization for the present reactivity studies. The approximate time to form rings and capsules from $\mathbf{U_1}$ as a function of the alkali are compiled in Figure 2, based on SAXS data (Figures 3a, S4). In summary, there is a distinct increase in solution reactivity with increasing alkali size, based on the rate of evolution to faces and capsules. Details about the Rb-$\mathbf{U_1}$ and Cs-$\mathbf{U_1}$ solution reactivity are described below since these are first reported here. In each study, Rb-$\mathbf{U_1}$ or Cs-$\mathbf{U_1}$ crystals were directly transferred from the crystallization solution to neat water for analysis, to avoid degradation in air.

The scattering data shows the dissolution of Rb-$\mathbf{U_1}$ in water results in the immediate assembly of larger species, with an average diameter of 12.1 Å, and radius of gyration of 4.4 Å (R_g, root mean squared average of scattering vectors in the molecule, Table S11). This is similar to the size of a pentameric face from the simulated scattering curve (Figure 3a, Table S11). The average diameter of species in solution after three days is 16.8 Å. At this point, precipitation ensues, leading to decreased scattering intensity at day 7 (solutions are filtered prior to analysis). Based on Raman spectroscopy, this insoluble precipitate appears to be $\mathbf{U_{32R}}$ (Figure S5).[20] Similar behavior was

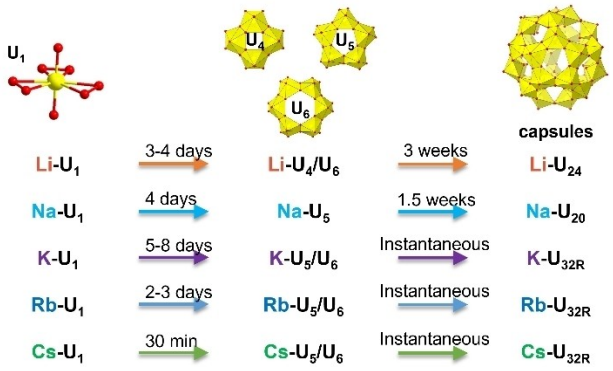

Figure 2. Summary of reaction rates of $\mathbf{U_1}$ compounds in solution, based on time to convert to topological faces (intermediates) and to capsules as determined by SAXS.

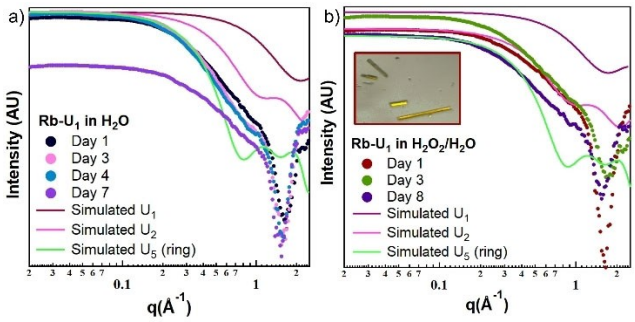

Figure 3. a) SAXS time study of Rb-$\mathbf{U_1}$ in H_2O and b) Rb-$\mathbf{U_1}$ in H_2O_2/H_2O mixture showing the different pathways to larger species. Three simulated scattering curves are shown for size comparison, $\mathbf{U_1}$ (magenta), $\mathbf{U_2}$ (pink), $\mathbf{U_5}$ (green). Inset in part b shows NaRb-$\mathbf{U_2}$ crystals obtained by vapor diffusion at day 1.

observed prior in the K-$\mathbf{U}_1$ system, but with a slower conversion rate (Figure 2).[11a] Like the reaction of K-$\mathbf{U}_1$, acicular needles are crystallized by vapor diffusion with ethanol and isopropyl alcohol, but the crystals from the Rb-solution are too thin and small to be mounted and analyzed by SCXRD. Given the similarities in morphology as the crystallized K-$\mathbf{U}_5$ [11a] and K-$\mathbf{U}_6$[11b] and the corollary SAXS data, we believe this is a pentameric or hexameric Rb^+ intermediate.

Dissolving Rb-$\mathbf{U}_1$ in water plus hydrogen peroxide slowed the evolution of Rb-$\mathbf{U}_1$, which consequently allowed the dimer, $\mathbf{U}_2$, to be observed in solution and isolated (Figure 3b, Table S12). By comparing the simulated to experimental scattering, $\mathbf{U}_1$ immediately evolves to $\mathbf{U}_2$ (Figure 3b), which is not observed in aqueous solutions without extra peroxide. Acicular crystals form by isopropyl alcohol diffusion on day 1 (Figure 3b, inset), identified as NaRb-$\mathbf{U}_2$. NaRb-$\mathbf{U}_2$ was previously reported by Kubatko with a slightly different unit cell.[21] Here, the dimer-structure 1) highlights the stepwise assembly of uranyl peroxide clusters, 2) benchmarks the dimer as an important intermediate as predicted by computation,[22] and 3) supports that peroxide decomposition is important in these solution phase reactions. In absence of vapor diffusion followed by $\mathbf{U}_2$ isolation, the species grow to pentamer/hexamer size (Table S12), followed by precipitation.

Characterization of Cs-$\mathbf{U}_1$ in solution was achieved by transferring Cs-$\mathbf{U}_1$ crystals directly from the mother liquor to neat water. We observe rapid conversion to larger species in solution by SAXS (Figures S4e, S4f, Table S13). Continued growth of soluble species is observed in a 4-day time period, but crystallization attempts for structure determination were unsuccessful.

Reaction of Hydrogen Peroxide with Alkali Hydroxide

The Rb-$\mathbf{U}_1$ and Cs-$\mathbf{U}_1$ solution studies presented here complete the reactivity trend of the uranyl triperoxide monomers, illustrating that Cs-$\mathbf{U}_1$ is the least stable in solution and undergoes polymerization immediately upon dissolution. To further explore and understand the role of the alkali in the destabilization of peroxide in $\mathbf{U}_1$, we documented the aqueous phase reaction between H_2O_2 and AOH using Raman spectroscopy, (Figures 4, S6–S7). We chose two AOH:H_2O_2 ratios to study; 1:2 and 1:3, 2.3 M AOH:4.2 M H_2O_2, and 1.8 M AOH:5.4 M H_2O_2, respectively (Table S1). Peroxide is in excess in this study so that the fastest reaction (with CsOH) can be quantified with some accuracy. Hydrogen peroxide has a Raman active O–O vibration, between 870–874 cm^{-1} (Figure 4a).[23] The evolution of O_2 gas is observed upon the addition of AOH to H_2O_2, and a second Raman peak appears at 850 cm^{-1}, with diminution of the H_2O_2 peak (874 cm^{-1}, Figure 4b). We have assigned the second peak to deprotonated hydrogen peroxide (HOO^-):

$$H_2O_2 + A^+ + OH^- \rightarrow HOO^- + A^+ + H_2O \quad (1)$$

The H_2O_2 peak (870 cm^{-1}) decreases over time while the peak at 850 cm^{-1} (HOO^-) rapidly reaches steady state. This

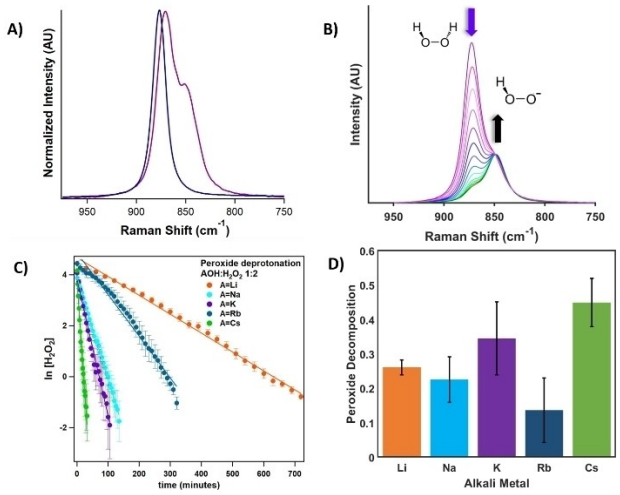

Figure 4. a) Raman spectra of 30 % $H_2O_{2(aq)}$ (blue) at 874 cm^{-1} and H_2O_2/$CsOH_{(aq)}$ (magenta) as an example mixture at time 0. b) Evolution of CsOH:H_2O_2 1:3 mixture (spectra for other AOH:H_2O_2 are compiled in Figure S6–S7). c) Rate of peroxide deprotonation ($H_2O_2^- \rightarrow HOO^-$) over time for a 1:2 AOH:H_2O_2 ratio (1:3 ratio shown in Figure S8). d) Total fraction of peroxide decomposed at the point of completion of the deprotonation reaction for the 1:2 A^+:H_2O_2 ratio (1:3 ratio shown in Figure S9).

suggests the first step of peroxide decomposition is deprotonation, followed by disproportionation, evolving oxygen.

$$HOO^- + A^+ \rightarrow 1/2O_{2(g)} + A^+ + OH^- \quad (2)$$

In theory, the reaction is 'pH neutral' since a hydroxide is consumed in step 1 and created in step 2. Because step 2, peroxide decomposition, does not go to completion (Figures 4d, S9), we might expect the pH to decrease. Instead, the pH goes up 1–2 units for each alkali (Table 1), suggesting there are other reaction pathways, and this may differ for different alkalis. In addition, peroxide decomposition produces more base, which can increase the overall reaction.

Table 1. Peroxide deprotonation rate, average reaction time, and initial and final pH for each AOH-H_2O_2 solution.

A^+	A^+:H_2O_2	*k* (rate of peroxide deprotonation[a])	Avg. reaction time[b,c]	Avg. initial pH[b,c]	Avg. final pH[b,c]	Δ pH
Li	1:2	0.007	720(1)	11.47(7)	12.22(4)	0.75
	1:3	0.010	690(4)	10.85(1)	11.76(1)	0.91
Na	1:2	0.040	145(1)	11.82(2)	13.15(1)	1.33
	1:3	0.056	150(7)	11.04(7)	12.87(2)	1.83
K	1:2	0.054	102(3)	11.81(2)	13.61(1)	1.80
	1:3	0.086	102(1)	11.45(6)	13.48(7)	2.03
Rb	1:2	0.016	326(5)	11.89(3)	13.66(2)	1.77
	1:3	0.017	420(2)	11.37(4)	13.52(2)	2.15
Cs	1:2	0.175	33(1)	11.87(10)	13.72(4)	1.85
	1:3	0.250	45(7)	11.20(25)	13.76(4)	2.56

[a] min^{-1}; [b] min, [c] error from triplicate measurements.

The assignment of the HOO^- peak was confirmed by dissolving Na_2O_2 in 0.4 M $H_2O_{2(aq)}$ since Na_2O_2 is not soluble in neat water (Figure S10). To this solution, we titrated 0.4 M HNO_3, and with each titration there is a decrease in the 850 cm^{-1} (deprotonated) peak and an increase in the 874 cm^{-1} (protonated) peak.

For the studied series, we deconvoluted the two peaks and determined the area under the curve for the 870 cm^{-1} (H_2O_2) peak as a function of time. The area under both peaks was normalized to the known peroxide starting concentration (Figures 4c, S8). Plotting $\ln[H_2O_2]$ against time gave plots with linear fitting of 97.0% or greater, except for the RbOH and LiOH experiments, indicating a first-order rate reaction with respect to the peroxide.[24] The first-order rate constant k is summarized in Table 1 for each studied solution, which corresponds to the rate of deprotonation of H_2O_2. In every case, except for Rb^+, the deprotonation rate is ~30–40% greater for the 1:3 ratio, likely due to the higher peroxide concentration (Table S1). The RbOH presented almost identical rates for both the 1:2 and 1:3 ratio solutions. Figure S11 shows exponential decrease of $[H_2O_2]$ vs. time plots, and Figures 4c and S8 show the $\log[H_2O_2]$ plots with time.

We also monitored total peroxide decomposed for both AOH:H_2O_2 ratios; the 1:3 ratios exhibit less total percent peroxide decomposed, since it has a higher starting concentration (Figures 4d, S9, Table S14). Any trend for this analysis is more subtle; however, the Rb-peroxide solutions exhibit remarkably less peroxide decomposition. We conclude that the RbOH contains an impurity that stabilizes peroxide. Based on the known impurities (Table S15), barium is most likely the culprit since it is known to form stable peroxide compounds as solids and complexes in solution.[25] Further, the impurities are likely excluded by crystallization of the Rb uranyl peroxide compounds, and therefore do not exhibit this same anomalous behavior as the RbOH solutions. Interestingly, the $\ln[H_2O_2]$ time plots suggest some equilibrium between species, evident in the bowing of curves. This suggests that there are multiple decomposition pathways in this complex reaction, which become more evident when the reaction is slow.

One hypothesis that could explain the profoundly different reactivity rates with peroxide between LiOH and CsOH is direct bonding of large alkalis with small hydration spheres (Cs^+) to peroxide in solution, promoting deprotonation, leading to faster decomposition. Further, direct bonding in solution can effectively destabilize the OOH^- anion by polarizing the O–O bond (whether bonded side-on or end-on), which promotes the second step of peroxide decomposition. Notably, consistent with the increased Δ pH down the series (Table 1), peroxide oxidation as a different decomposition mechanism could become increasingly important with increased A^+-peroxide bonding in solution; i.e., $O_2^{2-}{}_{(aq)} \rightarrow O_{2(g)} + 2e^-$, where the electrons react with H^+, increasing the pH. Finally, bonding of alkalis to peroxide in the A-$\mathbf{U_1}$ crystalline lattices increases down the alkali period (summarized in Figure 1), as does instability. The conversion of Cs-$\mathbf{U_1}$ involving partial reduction from U^{VI} to U^V supports this hypothesis.

Reaction of Cs Uranyl Triperoxide to Cesium Uranyl Tricarbonate via Direct Air Capture of CO_2

All attempts to stabilize Cs-$\mathbf{U_1}$ outside of the reaction solution for bulk characterization and further study was thwarted by conversion to a red-orange hygroscopic solid, with observed off-gassing from peroxide decomposition. The same was true for Rb-$\mathbf{U_1}$ and K-$\mathbf{U_1}$, but progressively slower with visual reaction rate Cs > Rb > K. Here, we study the decomposition of Cs-$\mathbf{U_1}$, initiated by simply removing the crystals from the reaction solution, grinding them in a mortar without adding solvent as grinding medium, and leaving them in open air (on a glass slide, watch glass, or in the mortar as shown in Figure 5b) for ~30 minute. The product can be obtained under a variety of conditions (i.e., aged in an oxygen-free glovebox, addition of a grinding solvent), but the above-reported process gave the cleanest and most consistent power X-ray diffraction results, our initial means of characterization. Notably, this intermediate material is constantly evolving toward its stable end-product of cesium uranyl tricarbonate (Figure 5c), and different characterization processes require different times for analysis and sample preparation. Therefore each characterization does not necessarily measure exactly the same material. As an additional caveat, attempts to remove reaction byproducts (i.e., CsOH) rendered the powder amorphous, which partially explains the inability to obtain a dry solid, since both CsOH and Cs uranates are hygroscopic.[26]

Discussion of this intermediate phase formation is below, and the characterization of uranyl tricarbonate is described here. It is far easier to isolate and characterize the uranyl tricarbonate phase than the intermediate phase, due to the stablity of the carbonate end-product. For example, crystals of suitable quality (Figure 5c) for SCXRD analysis grow from the red intermediate phase (Figure 5b). $Cs_4[UO_2(CO_3)_3 \cdot 6H_2O$ crystallizes in the $P2_1/n$ space group (Cs-$\mathbf{U_{1c}}$, Tables S2, S16, S17). In the unit cell, there is one unique $[UO_2(CO_3)_3]^{4-}$ anion, with U-O_{yl} distances of 1.780(1)–1.771(1) Å. The U-$O_{carbonate}$ bond distances are between 2.431(1)–2.472(1) Å. Similar to Rb-$\mathbf{U_1}$ and Cs-$\mathbf{U_1}$, the Cs^+ cations are directly bonded to the $[UO_2(CO_3)_3]^{4-}$ anion with Cs^+-O_{yl} bond lengths between 3.256(1)–3.629(1) Å, and Cs^+-$O_{carbonate}$ bond lengths between 2.965(1)–3.100(1) Å.

In a second experiment, we ground the Cs-$\mathbf{U_1}$ crystals with ethanol and transferred the slurry to a grid for TEM and selected area electron diffraction (details in SI). The grid was placed in a vacuum oven for 30 minutes to dry, to eliminate the degassing oxygen and water that would compromise the high vacuum. Anectodely and much to our surprise, the pressure of the vacuum chamber actually decreased rather than increased with introduction of the Cs-$\mathbf{U_1}$ decomposition product, a phenomenon rarely observed, which could be related to absorption/conversion of trace CO_2 to carbonate. Selected area electron diffraction revealed prior-reported anhydrous $Cs_4[UO_2(CO_3)_3]$,[27] shown in Figure 5c (asignment of diffraction spots is shown in Figure S12).

The diffractogram of the decomposed Cs-$\mathbf{U_1}$ crystals (Figure 5b) showed a surprisingly simple and clear pattern that did not match any reported U^{VI} oxide phases. However, it is a close

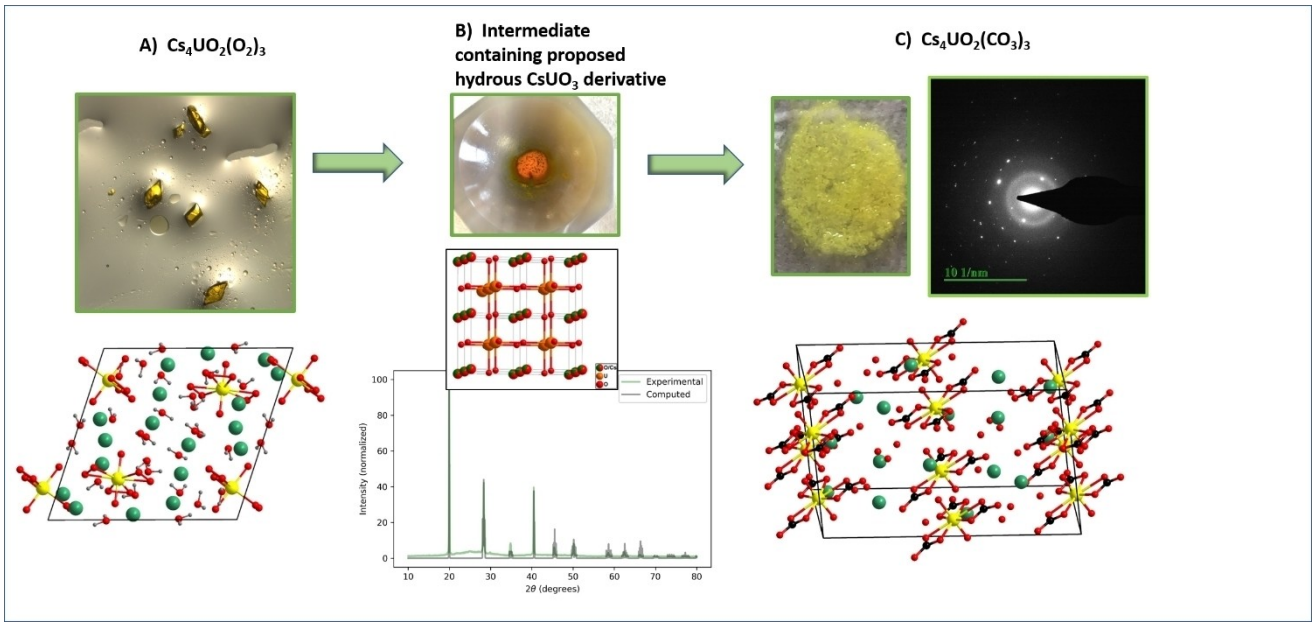

Figure 5. Overview of solid-state decomposition and characterization of Cs-$\mathbf{U_1}$. A) Microscope image of Cs-$\mathbf{U_1}$ crystals in oil prior to SCXRD (top), and representative view of the crystalline lattice (bottom). B) Photograph of Cs-$\mathbf{U_1}$ decomposed in air (top), simplified model of $(Cs,H_xO)UO_3$ (x = 2,3) (4:1 H_xO:Cs), a derivitive of computationally predicted $CsUO_3$ (middle, H's eliminated, see Figures S20–S23 for different orientations of hydrous molecules plus bending of U–O–U bond angles due to protonation and H-bonding); and simulated diffraction of this composition (black trace) compared to Cs-$\mathbf{U_1}$ decomposition product (green trace) (bottom). Protons of computated H_3O^+ migrate to framework O^{2-}, creating more chemically reasonable OH^- moieties, see text. C) Microscope image of $Cs_4UO_2(CO_3)_3 \cdot 6H_2O$ crystals (top left), view of the crystal lattice (bottom), and TEM-electron diffraction of Cs-$\mathbf{U_1}$ following grinding in solvent (top right). Diffraction spots index as prior-reported anhydrous $Cs_4[UO_2(CO_3)_3]$.[27] Labeled diffraction spots are shown in Figure S12.

match to the computationally predicted CsU^VO_3 perovskite (mp-865424), that features U^V on the B-site and Cs^+ on the A-site.[15] While AU^VO_3 perovskite has been reported for A=Li^+, Na^+, K^+, and Rb^+; synthesized by solid-state routes,[28] the Cs^+-analogue has thus far eluded synthesis, and instead mixed valence $Cs_2U_4O_{12}$ is obtained.[28b] Alkali U(V) oxides and oxyfluorides have also been obtained hydrothermally in alkaline hydroxide media.[29] Lebail fitting of the experimental diffraction data shows two unit cells, only slightly larger (2.4% by volume) than the computationally predicted phase (Figure S13, Table S18). Diffraction peaks are observable in air for up to ~4 hours before re-oxidizing to a purely U^{VI} phase, visually accompanied by transformation of the material from red-orange to yellow (Figure 5c). Within an argon-filled wet box, the transformation is slower; diffraction peaks persist for 1 week (Figure S14) but with diminished intensity.

Given the differential peak intensities between the computed and experimental $CsUO_3$ diffractograms (Figure S15), we considered (1) substitution of U^{VI} on the B-site, and (2) substitution of hydrous species (i.e., H_2O) on the A-site. In the calculated diffraction pattern, the peak at 28.6° (110) exhibits the highest intensity, while the experimental diffraction pattern has the most intense peak at 20.1° (001). The (111) peak at 35.2° is barely visible (but present) in the calculated diffraction pattern. Simulation of the diffractogram of $CsUO_3$ with the Cs-atom removed yields a diffraction pattern with relative peak intensities more consistent with the experimental pattern (Figure S16). The cubic δ-UO_3 lattice (MP-375) is similar to the $CsUO_3$ lattice, featuring corner-linked uranium (VI) octahedra (ReO_3-type lattice), but the A-site is vacant, and the unit cell of UO_3 is ~15% smaller due to the shorter U^{VI}-O bond lengths (compared to U^V-O bond lengths, Figure S16).

Computational Modeling of the Decomposed Cs-U_1 Phase

To determine the effect of phase composition on diffraction peak intensity of the decomposed Cs-$\mathbf{U_1}$, we embarked on an iterative computational exploration. The procedure is discussed at length in the SI, along with details of the density functional theory calculations using the Vienna Ab initio Simulation Package.[30] This interrogation yielded good agreement with the experimentally measured diffraction pattern for the Cs-$\mathbf{U_1}$ decomposition product (Figures 5b, S17). The density functional theory geometry relaxed structures demonstrate that introducing the H_xO (x = 2 and 3; respectively balancing U^{VI} and U^V) molecules at the A-sites introduces distortions to the cubic unit cell, in addition to the polyhedral distortions. The relative Cs:H_xO A-site occupation, as well as deviations of the α, β, and γ angles of the cubic lattice from 90°, all lead to improved match with the experimental pattern (Figure S17, Table S19).

To match the cell volume and peak intensities of the experimental diffraction pattern, we performed geometry optimization on three end-member lattice compositions: 1) $(H_2O)U^{VI}O_3$; 2) $(Cs,H_2O)U^{V/VI}O_3$; and 3) $(H_3O,Cs)U^VO_3$ as 2×2×2 supercells. A prior study provides experimental precedence for incorporation of hydrous species into related α-UO_3.[31] A 4:1 H_xO:Cs ratio proved ideal, based on closest agreement with the

experiment diffraction peak intensities (Figures 5b, S17), but we used a 3:1 ratio to remain commensurate with the eight A-sites in the computed 2×2×2 supercell. This supercell was chosen to accommodate a wider range of A-site substitutions and the octahedral distortions that result, as well as the computationally determined antiferromagnetic structure. We realize H_3O^+ is not a reasonable species in these basic media; however, during geometry optimization, the protons tended to migrate to the basic framework oxygens (creating hydroxides), and the framework stayed intact and within 10% of the experimentally observed volume (Table S20). While protonation of framework oxides increases cell volume by lengthening U–O bonds, bending of the U–O(H)–U bonds decreases cell volume (observed in Figure S20). Therefore, bridging hydroxides are a chemically reasonable moiety to consider as a means to charge-balance the lattice with variable $U^{V/VI}$. Further details concerning the computational studies are summarized in the SI, including Figures S19–S23 and Table S20.

Additional Characterization of the Transition from the Intermediate State to Cs Uranyl Carbonate

Since this intermediate phase undergoes rapid transition from $U^{VI}\rightarrow U^{V}\rightarrow U^{VI}$ (further evidence below) we will simply refer to it as Cs-$\mathbf{U_1}$ decomposition product hereforth, acknowledging uncertainty in speciation and composition with time. The prior work of Kravchuck[32] showed DAC behavior of potassium uranyl peroxide/superoxide complex known as 'KUPS'. Therefore we considered the role of adventitious superoxide in Cs-$\mathbf{U_1}$ in promoting the unusually high reactivity leading to formation of carbonate that we observed. We refer to possible superoxide as 'adventitious' because we did not promote its formation or stabilization in the synthesis. On the other hand, Kravchuck introduced superoxide and hydroperoxyl via addition of benzyl alcohol to uranyl nitrate dissolved in methanol to promote formation of the reactive oxygen species. The peroxide was introduced separately in a subsequent step to obtain the mixed ligands in KUPS. In our studies, electron paramagnetic resonance (EPR) analysis of various stages of decomposed Cs-$\mathbf{U_1}$ did not show any superoxide. The lack of superoxide is similar to our recent studies of DAC behavior of $V(O_2)_4^{3-}$; in which we detected ~5% superoxide present in the solid.[16] Peroxide alone bound to high-oxidation-state metals (U^{VI}, V^{V}) can undergo stabilization via DAC of CO_2; and the associated alkali does appear to affect the reaction rate. The f^1 electrons of U^{V} were not detected either, but computation predicts antiferromagnetic coupling, in agreement with previous experiments of related alkali metal uranate perovskites, AUO_3 ($A=Na^+$, K^+, Rb^+), that have also identified an antiferromagnetic ground-state in these materials.[26]

With lack of an EPR signal and computationally predicted antiferromagnetic coupling, we provide additional evidence for U^{V} in the Cs-$\mathbf{U_1}$ decomposition product via XPS. We could not obtain a spectrum of pristine Cs-$\mathbf{U_1}$ given its degradation behavior once removed from the mother liquor and brought into the vacuum chamber with sufficient low pressure. However, XPS analysis of the Cs-$\mathbf{U_1}$ decomposition product is consistent with prior-reported U(V) oxides, based on both the U*4f* peaks and the corresponding shake-up satellites that are associated to the intrinsic energy loss process[26,33] (Figure 6a). The full spectrum is shown in Figure S24, and fitted U*4f* peaks in Figure S25. The binding energy of the U$4f_{7/2}$ and U$4f_{5/2}$ peak for the Cs-$\mathbf{U_1}$ decomposition product is 380.6 eV (satellite at 389.8 eV), and at 391.5 eV (satellite at 400.3 eV), respectively (Figure 6). The 380.6 eV (U$4f_{7/2}$) peak is in a similar location to the reported peak for $NaUO_3$.[33a] The U$4f_{5/2}$ peak of the Cs-$\mathbf{U_1}$ decomposition product is also consistent with observed peaks in both $NaU^{V}O_3$ and $KU^{V}O_3$.[33a] Additional minor peaks are fitted (15% total integrated area), shown in Figure S25 and Table S21. These are likely the presence of U^{VI} substitution for U^{V} as discussed above or as impurity phases. XPS measurement of the same sample four hours later, when we are certain we have obtained the carbonate phase, reveals a shift in both U*4f* peaks to 381.3 (U$4f_{7/2}$) and 392.3 (U$4f_{5/2}$) eV. Both shifts are consistent with a $Cs_2U_4O_{13}$ standard that contains exclusively U^{VI}.[28c] Finally, an inorganic carbonate peak (*C1s*)[34] becomes more prominent in parallel with the U^{V} to U^{VI} peak shift (Figure 6b), indicating capture of atmospheric CO_2 as carbonate.

Finally, with Raman spectroscopy (Figure 7) we tracked the reaction of Cs-$\mathbf{U_1}$ to Cs-$\mathbf{U_{1c}}$ via the intermediate state. Assign-

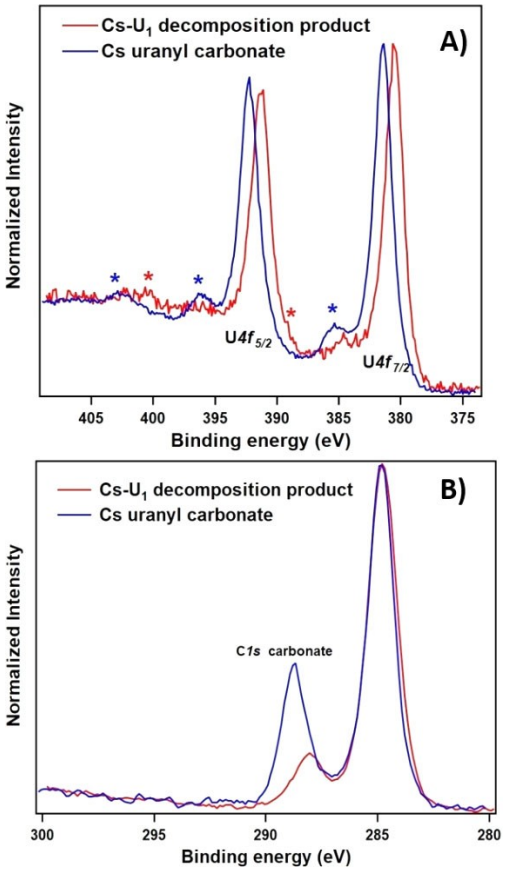

Figure 6. XPS analysis. A) shows the U *4f* peaks, B) shows the C 1s peaks. Red spectrum is the Cs-$\mathbf{U_1}$ initial decomposition product. Blue spectrum is the same material, several hours later, identified as $Cs_4[UO_2(CO_3)_3]$. Full spectra are shown in Figure S24.

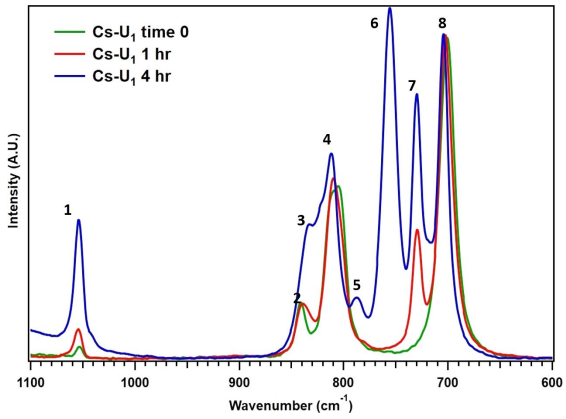

Figure 7. Tracking the degradation of Cs-$\mathbf{U_1}$ via Raman, intensity normalized to peak **8**. Peak positions (cm^{-1}) and possible assignments, some based on literature. **1**, 1054 (v_4-CO_3^{2-});[32] **2**, 840 (v_1-O_2^{2-}U);[32] **3**, 831 (v_3-CO_3^{2-});[32] **4**, 811 (U–O stretching);[35] **5**, 785 (unknown); **6**, 755 (v_1 UO_2^{2+} bound to CO_3^{2-}); **7**, 731 (O–U–O–U stretching or v_1 UO_2^{2+});[32,35] **8**, 704 (v_1 UO_2^{2+} bound to O_2^{2-}).

ments of some peaks were possible based on the literature; but again, there is ambiguity in the intermediate phase. The green spectrum, fresh Cs-$\mathbf{U_1}$ crystals, already exhibit a small CO_3^{2-} peak (**1**), suggesting this reaction begins immediately upon removing the crystals from the mother liquor. Peak **2** plus a double peak in the region of the peak labeled **4** are peroxide bound to uranyl of Cs-$\mathbf{U_1}$ (see Figure S26 for an expansion of this region), while the associated uranyl peak is labeled **8**. In the intermediate state (red spectrum), peaks **4** and **7** are consistent with Raman stretches observed for U_3O_8; a mixed $U^{V/VI}$ framework oxide with corner-sharing octahedra (similar to $CsUO_3$) and pentagonal bipyramids.[35] Peak **7** position has also been assigned as v_1 UO_2^{2+}.[32] Finally, peaks **1**, **3**, and **6** show a predominance of uranyl tricarbonate in the final decomposition state, the blue spectrum. Consistent withthe EPR studies, we observe no evidence for uranyl-bound superoxide, reported at 881 cm^{-1}.[32]

Conclusions

To date, the alkali cation of uranyl peroxide polyoxometalates was thought to participate in reactions via structure and solubility control only. Here, we have shown the alkali participates in reactivity, specifically by interacting with peroxide, driving decomposition, and in some cases altering reaction pathways. Li-$\mathbf{U_1}$ is stable for months (if refrigerated) in the solid state, and it undergoes polymerization to capsule forms in solution only with addition of a catalyst to activate peroxide decomposition.[9a] The Cs-$\mathbf{U_1}$ analogue demonstrates the other extreme–the solid survives less than 30 minutes outside its reaction solution, and in solution undergoes rapid conversion to insoluble capsules. Similarly, CsOH-promoted peroxide deprotonation (first step to decomposition) in the absence of uranyl exhibits a reaction rate more than double that of LiOH-promoted peroxide deprotonation. Hydrogen peroxide can act as either a reducing or oxidizing agent, normally an oxidizing agent in these alkaline solutions. We propose that Cs-$\mathbf{U_1}$ converts to a putative metastable U(V) intermediate in a hydrous derivative of computationally predicted (but never isolated) $CsUO_3$, likely reduced by peroxide. By DAC of CO_2, the intermediate phase then rapidly transforms to a stable U(VI) carbonate. Future and ongoing work includes understanding the role of alkalis in DAC when exploiting high-oxidation-state transition metals and f-block metals, with and without reactive oxygen species such as peroxide.

Supporting Information

Supporting information (SI) is available which contains experimental and computational details and additional Figures and tables as described throughout the text. Deposition numbers 2000559 (Rb-$\mathbf{U_1}$), 2000990 (NaRb-$\mathbf{U_2}$), 2000557 (Cs-$\mathbf{U_1}$), 2000558 (Cs-$\mathbf{U_2}$) and 2201209 (Cs-$\mathbf{U_{1C}}$) contain the supplementary crystallographic data for this paper. These data are provided free of charge by the joint Cambridge Crystallographic Data Centre and Fachinformationszentrum Karlsruhe Access Structures service. The authors have cited additional references within the Supporting Information (Ref. [20,27,36]).

Acknowledgements

The work performed at Oregon State University was supported by Department of Energy, Basic Energy Sciences under award DE-SC0022278. A.A. and TAK (Cs-$\mathbf{U_{1C}}$ structure) are grateful for the support of the Linus Pauling Distinguished Postdoctoral Fellowship program. RGS was supported the Department of Energy Office of Science, Office of Basic Energy Sciences, Division of Chemical Sciences, Geosciences and Biosciences, Heavy Element Chemistry program, FWP 73200. Pacific Northwest National Laboratory is a multiprogram laboratory operated by Battelle for the Department of Energy. G.M., M.K.H, and K.A.P (Berkeley) acknowledges support from the Department of Energy Computational Science Graduate Fellowship under grant DE-SC0020347. Computations in this paper were performed using resources of the National Energy Research Scientific Computing Center, a Department of Energy Office of Science User Facility operated under contract no. DE-AC02-05CH11231. High-throughput calculations, data, and software infrastructure was supported by the Department of Energy, Office of Science, Office of Basic Energy Sciences, Materials Sciences and Engineering Division under Contract DE- AC02-05CH11231: Materials Project program KC23MP. We gratefully acknowledge Jay LaVerne (UND), Casey Simons (UO), and Eric Walter (PNNL) for assistance in collecting EPR data that was not included in the final manuscript.

Conflict of Interests

The authors declare no conflict of interest.

Data Availability Statement

The data that support the findings of this study are available in the supplementary material of this article.

Keywords: uranyl · peroxide · alkalis · SAXS · X-ray structure · CO_2 direct air capture

[1] J. S. Hopkins, J. A. Golding, G. M. Ritcey, *Hydrometallurgy* **1987**, *17*, 315–334.
[2] P. C. Burns, K.-A. Hughes, *American Mineralogist* **2003**, *88*, 1165–1168.
[3] a) B. T. McGrail, L. S. Pianowski, P. C. Burns, *J. Am. Chem. Soc.* **2014**, *136*, 4797–4800; b) S. G. Thangavelu, C. L. Cahill, *Inorg. Chem.* **2015**, *54*, 4208–4221; c) D. V. Kravchuk, T. Z. Forbes, *Angew. Chem. Int. Ed.* **2019**, *58*, 18429–18433; d) A. S. Jayasinghe, L. C. Applegate, D. K. Unruh, J. Hutton, T. Z. Forbes, *Cryst. Growth Des.* **2019**, *19*, 1756–1766.
[4] P. C. Burns, K.-A. Kubatko, G. Sigmon, B. J. Fryer, J. E. Gagnon, M. R. Antonio, L. Soderholm, *Angew. Chem. Int. Ed.* **2005**, *44*, 2135–2139.
[5] a) P. C. Burns, M. Nyman, *Dalton Trans.* **2018**, *47*, 5916–5927; b) J. Qiu, P. C. Burns, *Chem. Rev.* **2013**, *113*, 1097–1120.
[6] a) G. E. Sigmon, J. Ling, D. K. Unruh, L. Moore-Shay, M. Ward, B. Weaver, P. C. Burns, *J. Am. Chem. Soc.* **2009**, *131*, 16648–16649; b) H. W. Kroto, J. R. Heath, S. C. O'Brien, R. F. Curl, R. E. Smalley, *Nature* **1985**, *318*, 162–163; c) G. E. Sigmon, D. K. Unruh, J. Ling, B. Weaver, M. Ward, L. Pressprich, A. Simonetti, P. C. Burns, *Angew. Chem. Int. Ed.* **2009**, *48*, 2737–2740.
[7] D. W. Lewis, A. R. Ruiz-Salvador, A. Gómez, L. M. Rodriguez-Albelo, F.-X. Coudert, B. Slater, A. K. Cheetham, C. Mellot-Draznieks, *CrystEngComm* **2009**, *11*, 2272–2276.
[8] a) P. Miró, S. Pierrefixe, M. Gicquel, A. Gil, C. Bo, *J. Am. Chem. Soc.* **2010**, *132*, 17787–17794; b) A. Gil, D. Karhánek, P. Miró, M. R. Antonio, M. Nyman, C. Bo, *Chem. Eur. J.* **2012**, *18*, 8340–8346; c) M. Nyman, T. M. Alam, *J. Am. Chem. Soc.* **2012**, *134*, 20131–20138.
[9] a) Z. Liao, T. Deb, M. Nyman, *Inorg. Chem.* **2014**, *53*, 10506–10513; b) T. M. Alam, Z. Liao, L. N. Zakharov, M. Nyman, *Chem. Eur. J.* **2014**, *20*, 8302–8307.
[10] M. Nyman, M. A. Rodriguez, T. M. Alam, *EurJIC* **2011**, *2011*, 2197–2205.
[11] a) A. Arteaga, L. Zhang, S. Hickam, M. Dembowski, P. C. Burns, M. Nyman, *Chem. Eur. J.* **2019**, *25*, 6087–6091; b) A. Arteaga, D. Ray, E. Glass, N. P. Martin, L. N. Zakharov, L. Gagliardi, M. Nyman, *Inorg. Chem.* **2020**, *59*, 1633–1641.
[12] L. Zhang, M. Dembowski, A. Arteaga, S. Hickam, N. P. Martin, L. N. Zakharov, M. Nyman, P. C. Burns, *Inorg. Chem.* **2019**, *58*, 439–445.
[13] a) N. W. Alcock, *J. Chem. Soc. A* **1968**, 1588–1594; b) M. Nyman, M. A. Rodriguez, C. F. Campana, *Inorg. Chem.* **2010**, *49*, 7748–7755.
[14] C. Falaise, M. Nyman, *Chem. Eur. J.* **2016**, *22*, 14678–14687.
[15] The Materials Project, https://next-gen.materialsproject.org/.
[16] E. G. Ribó, Z. W. Mao, J. S. Hirschi, T. Linsday, K. Bach, E. D. Walter, C. R. Simons, T. J. Zuehlsdorff, M. Nyman, *Chem. Sci.* **2024**, *15*, 1700–1713.
[17] M. Nyman, T. M. Alam, F. Bonhomme, M. A. Rodriguez, C. S. Frazer, M. E. Welk, *J. Cluster Sci.* **2006**, *17*, 197–219.
[18] C. R. Armstrong, M. Nyman, T. Shvareva, G. E. Sigmon, P. C. Burns, A. Navrotsky, *PNAS* **2012**, *109*, 1874–1877.
[19] M. Nyman, P. C. Burns, *Chem. Soc. Rev.* **2012**, *41*, 7354–7367.
[20] G. E. Sigmon, P. C. Burns, *J. Am. Chem. Soc.* **2011**, *133*, 9137–9139.
[21] K.-A. Kubatko, T. Z. Forbes, A. L. Klingensmith, P. C. Burns, *Inorg. Chem.* **2007**, *46*, 3657–3662.
[22] P. Miró, B. Vlaisavljevich, A. Gil, P. C. Burns, M. Nyman, C. Bo, *Chem. Eur. J.* **2016**, *22*, 8571–8578.
[23] a) V. Vacque, B. Sombret, J. P. Huvenne, P. Legrand, S. Suc, *SAA* **1997**, *53*, 55–66; b) D. T. Petkie, T. M. Goyette, F. C. De Lucia, P. Helminger, S. P. Belov, G. Winnewisser, *J. Mol. Spectrosc.* **1998**, *192*, 25–31.
[24] O. Špalek, J. Balej, I. Paseka, *J. Chem. Soc. Faraday Trans. 1* **1982**, *78*, 2349–2359.
[25] M. Königstein, C. R. A. Catlow, *J. Solid State Chem.* **1998**, *140*, 103–115.
[26] S. Van den Berghe, J. P. Laval, B. Gaudreau, H. Terryn, M. Verwerft, *J. Nucl. Mater.* **2000**, *277*, 28–36.
[27] S. V. Krivovichev, P. C. Burns, *Radiochemistry* **2004**, *46*, 12–15.
[28] a) Y. Hinatsu, *J. Alloys Compd.* **1994**, *203*, 251–257; b) A. B. Vanegmond, E. H. P. Cordfunke, *J. Inorg. Nucl. Chem.* **1976**, *38*, 2245–2247.
[29] a) Y. C. Chang, W. J. Chang, S. Boudin, K. H. Lii, *Inorg. Chem.* **2013**, *52*, 7230–7235; b) C. S. Lee, S. L. Wang, K. H. Lii, *J. Am. Chem. Soc.* **2009**, *131*, 15116–15117; c) C. H. Lin, K. H. Lii, *Angew. Chem. Int. Ed.* **2008**, *47*, 8711–8713; d) K. A. Pace, V. Kocevski, S. G. Karakalos, G. Morrison, T. Besmann, H. C. zur Loye, *Inorg. Chem.* **2018**, *57*, 4244–4247; e) J. T. Stritzinger, E. V. Alekseev, M. J. Polinski, J. N. Cross, T. M. Eaton, T. E. Albrecht-Schmitt, *Inorg. Chem.* **2014**, *53*, 5294–5299.
[30] J. Hafner, *J. Comput. Chem.* **2008**, *29*, 2044–2078.
[31] M. P. Wilkerson, S. C. Hernandez, W. T. Mullen, A. T. Nelson, A. L. Pugmire, B. L. Scott, E. S. Sooby, A. L. Tamasi, G. L. Wagner, J. R. Walensky, *Dalton Trans.* **2020**, *49*, 10452–10462.
[32] D. V. Kravchuk, N. N. Dahlen, S. J. Kruse, C. D. Malliakas, P. M. Shand, T. Z. Forbes, *Angew. Chem. Int. Ed.* **2021**, *60*, 15041–15048.
[33] a) J. H. Liu, S. Van den Berghe, M. J. Konstantinović, *J. Solid State Chem.* **2009**, *182*, 1105–1108; b) T. Gouder, R. Eloirdi, R. Caciuffo, *Sci. Rep.* **2018**, *8*, 8306.
[34] A. Shchukarev, D. Korolkov, *Open Chemistry* **2004**, *2*, 347–362.
[35] M. L. Palacios, S. H. Taylor, *Appl. Spectrosc.* **2000**, *54*, 1372–1378.
[36] a) CrysAlisPRO, Oxford Diffraction/Agilent Technologies UK Ltd, Yarnton, England, **2014**; b) L. J. Bourhis, O. V. Dolomanov, R. J. Gildea, J. A. K. Howard, H. Puschmann, *Acta Crystallogr. Sect. A* **2015**, *71*, 59–75; c) M. S. Christian, E. R. Johnson, T. M. Besmann, *J. Phys. Chem.* **2021**, *125*, 2791–2799; d) O. V. Dolomanov, L. J. Bourhis, R. J. Gildea, J. A. K. Howard, H. Puschmann, *J. Appl. Crystallogr.* **2009**, *42*, 339–341; e) J. Ilavsky, P. R. Jemian, *J. Appl. Crystallogr.* **2009**, *42*, 347–353; f) E. B. Jones, V. Stevanović, *npj Comput Mater* **2020**, *6*, 56; g) D. Kriegner, E. Wintersberger, J. Stangl, *J. Appl. Crystallogr.* **2013**, *46*, 1162–1170; h) A. C. Larson, R. B. Von Dreele, *Los Alamos, New Mexico: Los Alamos National Laboratory* **2004**; i) G. Sheldrick, *Acta Crystallogr. Sect. C* **2015**, *71*, 3–8; j) G. Sheldrick, *Acta Crystallogr. Sect. A* **2015**, *71*, 3–8; k) B. Toby, *J. Appl. Crystallogr.* **2001**, *34*, 210–213; l) P. F. Weck, C. F. Jové-Colón, E. Kim, *Phys. Chem. Chem. Phys.* **2019**, *21*, 25569–25576; m) X. B. Zuo, G. L. Cui, K. M. Merz, L. G. Zhang, F. D. Lewis, D. M. Tiede, *P Natl Acad Sci USA* **2006**, *103*, 3534–3539; n) S. Grimme, J. Antony, S. Ehrlich, H. Krieg, *Chem. Phys.* **2010**, *132*, 154104.

Manuscript received: February 17, 2024
Accepted manuscript online: March 11, 2024
Version of record online: April 3, 2024